# A Reynolds–uniform numerical method for Prandtl's boundary layer problem for flow past a plate with mass transfer

J.S. Butler

Department of Mathematics, Trinity College, Dublin, Ireland.

J.J.H Miller

Department of Mathematics, Trinity College, Dublin, Ireland

G.I. Shishkin

Institute for Mathematics and Mechanics, Russian Academy of Sciences, Ekaterinburg, Russia

**Abstract**

In this paper we consider Prandtl's boundary layer problem for incompressible laminar flow past a plate with transfer of fluid through the surface of the plate. When the Reynolds number is large the solution of this problem has a parabolic boundary layer. In a neighbourhood of the plate the solution of the problem has an additional singularity which is caused by the absence of the compartability conditions. To solve this problem outside nearest neighbourhood of the leading edge, we construct a direct numerical method for computing approximations to the solution of the problem using a piecewise uniform mesh appropriately fitted to the parabolic boundary layer. To validate this numerical method, the model Prandtl problem with self-similar solution was examined, for which a *reference* solution can be computed using the Blasius problem for a nonlinear ordinary differential equation. For the model problem, suction/blowing of the flow rate density is $v_0(x) = -v_i 2^{-1/2} Re^{1/2} x^{-1/2}$, where the Reynolds number $Re$ can be arbitrarily large and $v_i$ is the intensity of the mass transfer with arbitrary values in the segment $[-.3, .3]$. We considered the Prandtl problem in a finite rectangle excluding the leading edge of the plate for various values of $Re$ which can be arbitrary large and for some values of $v_i$, when meshes with different number of mesh points were used. To find reference solutions for the the velocity components and their derivatives with required accuracy, we solved the Blasius problem using a semi–analytical numerical method. By extensive numerical experiments we showed that the direct numerical method constructed in this paper allows us to approximate both the solution and its derivatives $Re$–uniformly for different values of $v_i$.

**Keywords:**

boundary layer equations, Prandtl's problem with mass transfer, Reynolds uniform direct numerical method, finite difference.

# 1 Introduction

Incompressible laminar flow past a semi-infinite plate P with mass transfer in the domain $D = \mathbf{R}^2$ is governed by the Navier-Stokes equations. Using Prandtl's approach the vertical momentum equation is omitted and the horizontal momentum equation is simplified, see [2] and [3]. For large Reynolds numbers the new momentum equation is parabolic and singularly perturbed, which means that the highest order derivative is multiplied by a small singular perturbation parameter $\varepsilon = \frac{1}{Re}$.

It is well known that for flow problems with large Reynolds numbers a boundary layer arises on the surface of the plate. Also, when classical numerical methods are applied to these problems large errors occur, especially in approximations of the derivatives, which grow unboundedly as the Reynolds number increases. For this reason robust layer-resolving numerical methods, in which the error is independent of the singular perturbation parameter, are required. Here we solve the Prandtl problem in a region including the parabolic boundary layer. Since the solution of the problem has another singularity at the leading edge of the plate we take as the computational domain the finite rectangle $\Omega = (.1, 1.1) \times (0, 1)$ on the upper side of the plate, sufficiently far from the leading edge (see Fig. 1) such that the leading edge singularity does not cause excessive problems for the numerical method. We denote the boundary of $\Omega$ by $\Gamma = \Gamma_L \bigcup \Gamma_T \bigcup \Gamma_B \bigcup \Gamma_R$ where $\Gamma_L$, $\Gamma_T$, $\Gamma_B$ and $\Gamma_R$ denote, respectively the left-hand, top, bottom and right-hand edges of $\Omega$.

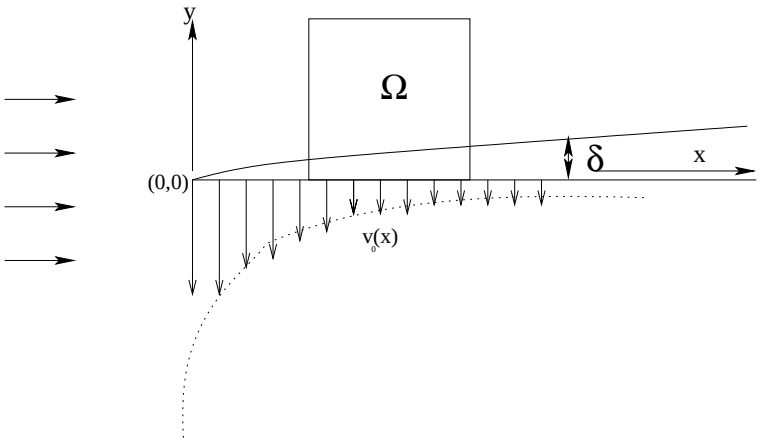


Figure 1: Flow past a plate with suction/blowing.

In figure 1 we see the constant flow to the left hand side of the plate, along the plate $\delta$ denotes the width of the boundary layer and $v_0(x)$ denotes the mass transfer.

The Prandtl boundary layer problem in $D$ is:

$$(P_\varepsilon)\begin{cases}\text{Find } \mathbf{u}_\varepsilon = (u_\varepsilon, v_\varepsilon) \text{ such that for all } (x,y) \in D \\ \\ \mathbf{u}_\varepsilon \text{ satisfies the differential equation} \\ \\ -\frac{1}{Re}\frac{\partial^2 u_\varepsilon}{\partial^2 y} + \mathbf{u}_\varepsilon.\nabla u_\varepsilon = 0 \\ \\ \nabla.\mathbf{u}_\varepsilon = 0 \\ \\ \text{with boundary conditions} \\ \\ u_\varepsilon = 0 \text{ and } v_\varepsilon = v_0(x) \text{ on } \Gamma_B \\ \\ \mathbf{u}_\varepsilon = \mathbf{u}_P \text{ on } \Gamma_L \bigcup \Gamma_T\end{cases}$$

where $v_0(x)$ is the velocity normal to the plate at which mass is transferred through its surface (see eqn (1) in section 2). The case for no mass transfer, $v_0(x) = 0$, was dealt with in [1] and it was used a the starting point for this paper.

We construct a numerical method for which there are error bounds for the solution components and their derivatives, such that the error constants do not depend on the value of $Re$ or $v_i$, where $v_i$ is the intensity of the mass transfer. That is, the method is $(Re, v_i)$–uniform.

## 2 Semi-analytical solution

Using the transformation described in [4], a self similar solution $\mathbf{u_B} = (u_B, v_B)$ of $(P_\varepsilon)$ can be written in the form

$$u_B = f^{'}(\eta)$$

$$v_B = \frac{1}{2}\sqrt{\frac{2}{xRe}}(\eta f^{'}(\eta) - f(\eta))$$

where

$$\eta = y\sqrt{\frac{Re}{2x}}$$

and the function f is the solution to the Blasius problem

$$(P_B)\begin{cases}\text{Find } f \in C^3([0,\infty)) \text{ such that for all } \eta \in [0,\infty) \\ \\ f^{'''}(\eta) + f(\eta)f^{''}(\eta) = 0 \\ \\ f(0) = v_i, \quad f^{'}(0) = 0, \quad \lim_{\eta\to\infty} f^{'}(\eta) = 1\end{cases}$$

In [5] the Blasius problem $(P_B)$ is solved numerically for the function $f$, and the relations are used to construct the Blasius solution $\mathbf{u_B}$ of $P_\varepsilon$. From [4] we have

$$v_0(x) = -v_i\sqrt{\frac{Re}{2x}} \tag{1}$$

Negative values of $v_i$ correspond to injection, positive values correspond to suction. Technically $v_i$ can have $(-\infty, \infty)$, but in practice when $v_i \leq -0.87$ the boundary layer is blown away from the surface. In addition to this there is an upper limit of 7.07 [2]. The Blasius equation with no mass transfer, $v_i = 0$, was dealt with in [1].

The purpose of finding this Blasius solution of Prandtl's problem is that we use it as a reference solution for the unknown exact solution in the expression for the error, when we estimate the error in the direct method of the next section. In this way, since the Blasius solution is known to converge Reynolds–uniformly to the solution of Prandtl's problem and we can estimate guaranteed error bounds for it [5].

# 3 Nonlinear direct finite difference method

In this section we begin to construct a robust numerical method to solve the Prandtl problem $(P_\varepsilon)$ for all admissible values of Reynolds numbers $Re$ and $v_i \in [-0.3, 0.3]$.

We define the rectangular mesh as in [1] on the rectangle $\Omega$ to be the tensor product of two one–dimensional meshes $\Omega_\varepsilon^{\mathbf{N}} = \Omega_\varepsilon^{N_x} \times \Omega_\varepsilon^{N_y}$, where $\mathbf{N}=(N_x, N_y)$. The mesh in the x direction is the uniform mesh

$$\Omega_\varepsilon^{N_x} = \{x_i : x_i = 0.1 + iN_x^{-1}, 0 \leq i \leq N_x\}.$$

The mesh in the y-direction is the piecewise–uniform fitted mesh

$$\Omega_\varepsilon^{N_y} = \{y_j : y_j = \sigma j \frac{2}{N_y}, 0 \leq j \leq \frac{N_y}{2}; y_j = \sigma + (1-\sigma)(j - \frac{N_y}{2})\frac{2}{N_y}, \frac{N_y}{2} \leq j \leq N_y\}.$$

It is important to note the position of the boundary layer in order to define an appropriate transition point $\sigma$ from the coarse to the fine mesh, so that there is a fine mesh in the boundary layer. The appropriate choice in this case is

$$\sigma = \min\{\frac{1}{2}, \sqrt{\varepsilon} ln N_y\}. \tag{2}$$

The factor $\sqrt{\varepsilon}$ may be motivated from *a priori* estimates of the derivatives of the solution $\mathbf{u}_\varepsilon$ or from asymptotic analysis. For simplicity we take $N_x = N_y = N$ (see Fig 2).

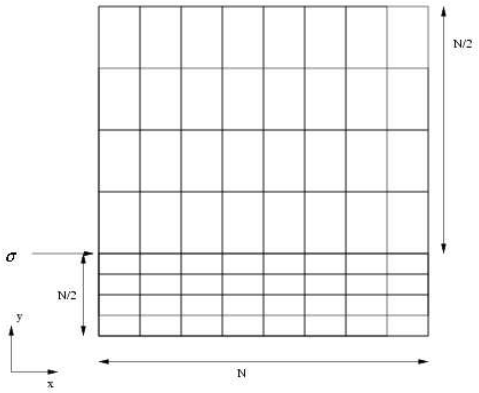


Figure 2: 2-d mesh constructed from a tensor product.

Using the above piecewise uniform fitted mesh $\Omega_\varepsilon^{\mathbf{N}}$ the problem $(P_\varepsilon)$ is discretized by the following nonlinear system of upwind finite difference equations for the approximation velocity components $\mathbf{U}_\varepsilon = (U_\varepsilon, V_\varepsilon)$

$$(P_\varepsilon^{\mathbf{N}}) \begin{cases} \text{Find } \mathbf{U}_\varepsilon = (U_\varepsilon, V_\varepsilon) \text{ such that for all } (x_i, y_j) \in \Omega_\varepsilon^{\mathbf{N}} \\ (-\varepsilon\delta_y^2 + \mathbf{U}_\varepsilon \cdot \mathbf{D}^-)U_\varepsilon(x_i, y_j) = 0 \\ (\mathbf{D}^- \cdot \mathbf{U}_\varepsilon)(x_i, y_j) = 0 \\ U_\varepsilon = 0, \quad V_\varepsilon = v_0(x_i) \text{ on } \Gamma_B \\ U_\varepsilon = U_B \text{ on } \Gamma_L \bigcup \Gamma_T \end{cases}$$

where $\mathbf{D}^- = (D_x^-, D_y^-)$, $D_x^-$ and $D_y^-$ are standard backward difference operators, and $\delta_y^2$ is a standard central difference operator.

# 4 Iterative direct finite difference method

Since the problem $(P_\varepsilon^{\mathbf{N}})$ is a nonlinear system an iterative method is required for its solution. This is obtained by replacing the system of nonlinear equations with a sequence of systems of linear equations, this is an adaptation of the method used in [1]. The systems of linearized equations are

$$
(A_\varepsilon^{\mathbf{N}})\ \begin{cases}
\text{With the boundary condition } \mathbf{U}_\varepsilon^{\mathbf{M}} = \mathbf{U}_{\mathbf{B}}^{\mathbf{8192}} \text{ on } \Gamma_L, \\
\text{for each } i, 1 \le i \le N, \text{ use the initial guess } \mathbf{U}_\varepsilon^0|_{X_i} = \mathbf{U}_\varepsilon^{M_{i-1}}|_{X_{i-1}} \\
\text{and for } \ m = 1, \ldots, M_i \ \text{ solve the following} \\
\text{two point boundary value problem for } U_\varepsilon^m(x_i, y_j) \\
(-\varepsilon\delta_y^2 + \mathbf{U}_\varepsilon^{m-1} \cdot \mathbf{D}^-)U_\varepsilon^m(x_i, y_j) = 0, \quad 1 \le j \le N-1 \\
\text{with the boundary conditions } U_\varepsilon^m = U_B \text{ on } \Gamma_B \cup \Gamma_T, \\
\text{and the initial guess for } V_\varepsilon^0|_{X_1} = 0. \\
\text{Also solve the initial value problem for } V_\varepsilon^m(x_i, y_j) \\
(\mathbf{D}^- \cdot \mathbf{U}_\varepsilon^m)(x_i, y_j) = 0, \\
\text{with initial condition } V_\varepsilon^m = v_0(x_i) \text{ on } \Gamma_B. \\
\text{Continue to iterate between the equations for } \mathbf{U}_\varepsilon^m \text{ until } m = M_i, \\
\text{where } M_i \text{ is such that} \\
\max\big(|U_\varepsilon^{M_i} - U_\varepsilon^{M_i-1}|_{\overline{X}_i}, \frac{1}{V^*}|V_\varepsilon^{M_i} - V_\varepsilon^{M_i-1}|_{\overline{X}_i}\big) \le tol.
\end{cases}
$$

For notational simplicity, we suppress explicit mention of the iteration superscript $M_i$ henceforth, and we write simply $\mathbf{U}_\varepsilon$ for the solution generated by $(A_\varepsilon^{\mathbf{N}})$. We take $tol = 10^{-6}$ in the computations. We note that there are no known theoretical results concerning the convergence of the solutions $\mathbf{U}_\varepsilon$ of $(P_\varepsilon^{\mathbf{N}})$ to the solution $\mathbf{u}_\varepsilon$ of $(P_\varepsilon)$ and no theoretical estimate for the pointwise error $(\mathbf{U}_\varepsilon - \mathbf{u}_\varepsilon)(x_i, y_j)$. It is for this reason that we are forced to apply controllable experimental techniques, which are adapted to the problem under consideration and are of crucial value to our understanding of the computational problems. $V^*$ is defined to be

$$V^* = \max_{\Omega_\varepsilon^N} V_B. \tag{3}$$

# 5 Error Analysis for the iterative direct method

In this section we compute Reynolds–uniform maximum pointwise errors in the approximations generated by the direct numerical method described in the previous section. For the sake of brevity, we show the errors for only the two extreme values of mass transfer in the set we are dealing with, $v_i = 0.3$ and two tables for $v = -0.3$ as the quality behaviour of errors and convergence orders are qualitatively the same as they are for $v_i = 0.3$. We compare the parameter uniform maximum pointwise errors in the approximations generated by the direct numerical method of the previous section with the corresponding semi–analytic values of section 2. We use the following definitions for the errors

$$E_\varepsilon^{\mathbf{N}}(U_\varepsilon) = ||U_\varepsilon - \overline{U_B}^{8192}||_{\overline{\Omega}_\varepsilon^N}$$

$$E_\varepsilon^{\mathbf{N}}(\frac{1}{V^*}V_\varepsilon) = \frac{1}{V^*}||V_\varepsilon - \overline{V_B}^{8192}||_{\overline{\Omega}_\varepsilon^N}$$

where $V^*$ is defined as in eqn(3).

Graphs of the scaled discrete velocity components generated by $(A_\varepsilon^{\mathbf{N}})$ are given for N=32, $\varepsilon = 1.0$ and $2^{-12}$ and $v_i = 0.3$ and $-0.3$ in figure 3, 4 and 5 For small Reynolds the velocity components are smooth which is shown in fig 3.

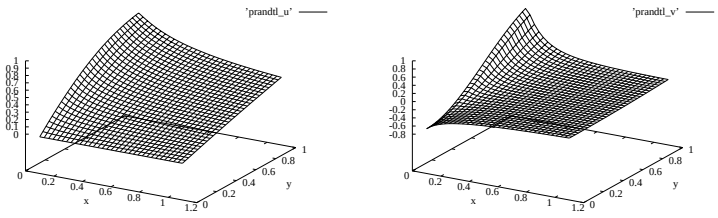


Figure 3: Graphs of $U_\varepsilon$ and $\frac{1}{V^*}(V_\varepsilon)$ for $\varepsilon = 1.0$, N=32 and $v_i = 0.3$.

In figs 4 and 5 we see that there is rapid change in a small region along the plate for the scaled velocity components with $v_i = 0.3$ and $-0.3$.

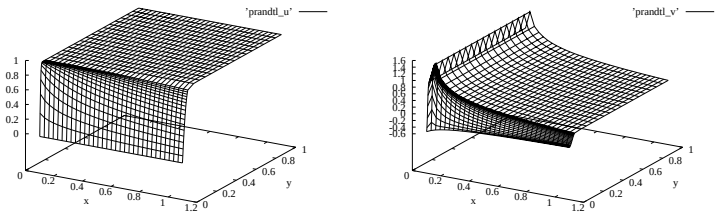


Figure 4: Graphs of $U_\varepsilon$ and $\frac{1}{V^*}(V_\varepsilon)$ for $\varepsilon = 2^{-12}$, N=32 and $v_i = 0.3$.

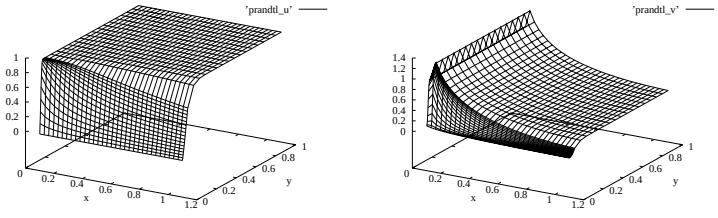


Figure 5: Graphs of $U_\varepsilon$ and $\frac{1}{V^*}(V_\varepsilon)$ for $\varepsilon = 2^{-12}$, N=32 and $v_i = -0.3$.

In figure 5 we see that in the top right hand corner of the graph of $U_\varepsilon$ that the transition point (eqn (2)) of the mesh $\Omega_\varepsilon^{\mathbf{N}}$ is slightly smaller than the width

of the layer this is due to the effect of the mass transfer blowing the boundary layer out.

| $\varepsilon \backslash N$ | 8 | 16 | 32 | 64 | 128 | 256 | 512 |
|---|---|---|---|---|---|---|---|
| $2^{-0}$ | 1.82e-03 | 1.90e-03 | 1.17e-03 | 7.36e-04 | 3.98e-04 | 2.63e-04 | 1.37e-04 |
| $2^{-2}$ | 3.19e-02 | 1.54e-02 | 7.48e-03 | 3.69e-03 | 1.81e-03 | 8.77e-04 | 4.09e-04 |
| $2^{-4}$ | 7.72e-02 | 3.23e-02 | 1.53e-02 | 7.48e-03 | 3.69e-03 | 1.82e-03 | 8.79e-04 |
| $2^{-6}$ | 7.93e-02 | 4.53e-02 | 2.62e-02 | 1.48e-02 | 7.36e-03 | 3.67e-03 | 1.82e-03 |
| $2^{-8}$ | 7.67e-02 | 4.53e-02 | 2.62e-02 | 1.54e-02 | 8.96e-03 | 5.14e-03 | 2.90e-03 |
| . | . | . | . | . | . | . | . |
| $2^{-20}$ | 1.53e-01 | 6.77e-02 | 2.62e-02 | 1.54e-02 | 8.96e-03 | 5.14e-03 | 2.90e-03 |
| $E^N$ | 1.53e-01 | 6.77e-02 | 2.62e-02 | 1.54e-02 | 8.96e-03 | 5.14e-03 | 2.90e-03 |

Table 1: Computed maximum pointwise error $E_\varepsilon^{\mathbf{N}}(U_\varepsilon)$ where $U_\varepsilon$ is generated by $(A_\varepsilon^{\mathbf{N}})$ for various values of $\varepsilon$, $N$ and $v_i$=0.3.

| $\varepsilon \backslash N$ | 8 | 16 | 32 | 64 | 128 | 256 | 512 |
|---|---|---|---|---|---|---|---|
| $2^{-0}$ | 4.06e-01 | 2.73e-01 | 1.54e-01 | 7.71e-02 | 3.84e-02 | 1.79e-02 | 8.71e-03 |
| $2^{-2}$ | 5.41e-01 | 3.39e-01 | 1.91e-01 | 1.03e-01 | 5.56e-02 | 3.04e-02 | 1.69e-02 |
| $2^{-4}$ | 1.48e+00 | 6.72e-01 | 3.40e-01 | 1.85e-01 | 1.04e-01 | 5.86e-02 | 3.32e-02 |
| $2^{-6}$ | 1.57e+00 | 1.03e+00 | 6.41e-01 | 3.79e-01 | 2.10e-01 | 1.19e-01 | 6.76e-02 |
| $2^{-8}$ | 1.52e+00 | 1.03e+00 | 6.41e-01 | 3.98e-01 | 2.59e-01 | 1.68e-01 | 1.08e-01 |
| . | . | . | . | . | . | . | . |
| $2^{-20}$ | 1.44e+00 | 1.03e+00 | 6.40e-01 | 3.98e-01 | 2.59e-01 | 1.68e-01 | 1.08e-01 |
| $E^N$ | 1.57e+00 | 1.03e+00 | 6.41e-01 | 3.98e-01 | 2.59e-01 | 1.68e-01 | 1.08e-01 |

Table 2: Computed maximum pointwise error $E_\varepsilon^{\mathbf{N}}(\frac{1}{V^*}V_\varepsilon)$ where $V_\varepsilon$ is generated by $(A_\varepsilon^{\mathbf{N}})$ for various values of $\varepsilon$, $N$ and $v_i$=0.3.

Tables 1 and 2 are the errors of the scaled velocity components generated by $(A_\varepsilon^{\mathbf{N}})$, for various values of N and Reynolds with $v_i = 0.3$. From the tables we see for each given N as Reynolds increases the error becomes constant with respect to Reynolds, we will refer to this as stabilising.

| $\varepsilon \backslash N$ | 8 | 16 | 32 | 64 | 128 | 256 | 512 |
|---|---|---|---|---|---|---|---|
| $2^{-0}$ | 4.49e-03 | 5.27e-03 | 4.19e-03 | 2.45e-03 | 1.33e-03 | 6.95e-04 | 3.98e-04 |
| $2^{-2}$ | 3.09e-02 | 1.94e-02 | 1.11e-02 | 5.98e-03 | 3.10e-03 | 1.59e-03 | 8.20e-04 |
| $2^{-4}$ | 2.94e-01 | 1.24e-01 | 5.74e-02 | 2.77e-02 | 1.37e-02 | 6.80e-03 | 3.43e-03 |
| $2^{-6}$ | 3.93e-01 | 1.87e-01 | 9.89e-02 | 5.28e-02 | 2.54e-02 | 1.25e-02 | 6.24e-03 |
| $2^{-8}$ | 4.59e-01 | 2.17e-01 | 9.94e-02 | 5.49e-02 | 3.06e-02 | 1.70e-02 | 9.43e-03 |
| . | . | . | . | . | . | . | . |
| $2^{-20}$ | 2.57e-01 | 1.66e-01 | 9.75e-02 | 5.49e-02 | 3.06e-02 | 1.70e-02 | 9.43e-03 |
| $E^N$ | 4.59e-01 | 2.17e-01 | 9.94e-02 | 5.49e-02 | 3.06e-02 | 1.70e-02 | 9.43e-03 |

Table 3: Computed maximum pointwise error $E_\varepsilon^{\mathbf{N}}(U_\varepsilon)$ where $U_\varepsilon$ is generated by $(A_\varepsilon^{\mathbf{N}})$ for various values of $\varepsilon$, $N$ and $v_i$=-0.3.

Table 3 is the error values of the scaled velocity component in the x direction generated by $(A_\varepsilon^{\mathbf{N}})$ for various values of N and Reynolds with $v_i = -0.3$. As

with the previous tables the error stabilises as Reynolds increases.

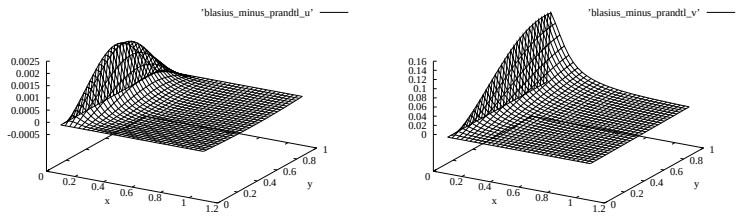


Figure 6: Graphs of $U_\varepsilon - U_B^{8192}$ and $\frac{1}{V^*}(V_\varepsilon - V_B^{8192})$ for $\varepsilon = 1.0$, N=32 and $v_i = 0.3$.

Graphs of the differences $U_\varepsilon - U_B^{8192}$ and $\frac{1}{V^*}(V_\varepsilon - V_B^{8192})$ for $\varepsilon = 1.0$, N=32 with $v_i = 0.3$ are smooth as shown in fig 6.

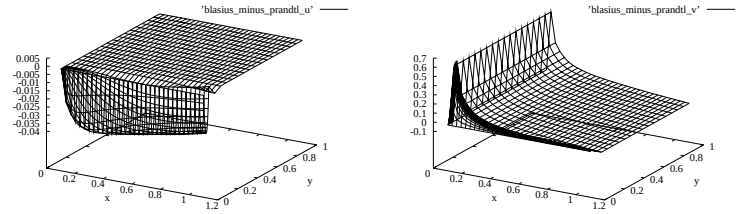


Figure 7: Graphs of $U_\varepsilon - U_B^{8192}$ and $\frac{1}{V^*}(V_\varepsilon - V_B^{8192})$ for $\varepsilon = 2^{-12}$, N=32 and $v_i = 0.3$.

For large Reynolds numbers the boundary layer arises, due to this rapid change of velocity in a small region, the error is localised in the boundary layer for both $U_\varepsilon$ and $\frac{1}{V^*}V_\varepsilon$ for N=32 and $\varepsilon = 2^{-12}$ for $v_i = 0.3$ (see fig 7 ).
We now estimate the orders of convergence of the numerical approximations generated by the direct numerical method, by introducing the computed orders of convergence using the definition from [1] they are

$$p^N_{\varepsilon,comp} = log_2 \frac{||U^N_\varepsilon - U^{8192}_B||_{\Omega^N_\varepsilon}}{||U^{2N}_\varepsilon - U^{8192}_B||_{\Omega^{2N}_\varepsilon}}$$

and $p^N_{comp}$ by

$$p^N_{comp} = log_2 \frac{max_\varepsilon ||U^N_\varepsilon - U^{8192}_B||_{\Omega^N_\varepsilon}}{max_\varepsilon ||U^{2N}_\varepsilon - U^{8192}_B||_{\Omega^{2N}_\varepsilon}}$$

with corresponding definitions for the scaled components.

| $\varepsilon \backslash N$ | 8 | 16 | 32 | 64 | 128 | 256 |
|---|---|---|---|---|---|---|
| $2^{-0}$ | -0.07 | 0.71 | 0.67 | 0.92 | 0.76 | 1.04 |
| $2^{-2}$ | 1.12 | 1.05 | 1.03 | 1.02 | 1.03 | 1.05 |
| $2^{-4}$ | 1.45 | 1.18 | 1.08 | 1.04 | 1.03 | 1.03 |
| $2^{-6}$ | 1.01 | 0.90 | 0.92 | 1.07 | 1.04 | 1.02 |
| $2^{-8}$ | 1.00 | 0.90 | 0.87 | 0.85 | 0.85 | 0.85 |
| . | . | . | . | . | . | . |
| $2^{-20}$ | 1.04 | 1.03 | 0.87 | 0.85 | 0.85 | 0.85 |
| $p^N_{comp}$ | 1.04 | 1.03 | 0.87 | 0.85 | 0.85 | 0.85 |

Table 4: Computed orders of convergence $p^N_{\varepsilon,comp}$, $p^N_{comp}$ for $U_\varepsilon - U_B^{8192}$ where $U_\varepsilon$ is generated by $(A^{\mathbf{N}}_\varepsilon)$ for various values of $\varepsilon$, $N$ and $v_i$=0.3.

Tables 4 – 5 indicate the order of convergence for $U_\varepsilon$ is at least 0.8 and 0.6 for $\frac{1}{V^*}(V_\varepsilon)$ for $v_i = 0.3$ and all Reynolds.

| $\varepsilon \backslash N$ | 8 | 16 | 32 | 64 | 128 | 256 |
|---|---|---|---|---|---|---|
| $2^{-0}$ | 0.57 | 0.83 | 1.00 | 1.01 | 1.10 | 1.04 |
| $2^{-2}$ | 0.67 | 0.83 | 0.89 | 0.89 | 0.87 | 0.85 |
| $2^{-4}$ | 1.14 | 0.98 | 0.87 | 0.84 | 0.82 | 0.82 |
| $2^{-6}$ | 0.61 | 0.69 | 0.76 | 0.86 | 0.82 | 0.81 |
| $2^{-8}$ | 0.56 | 0.68 | 0.69 | 0.62 | 0.62 | 0.64 |
| . | . | . | . | . | . | . |
| $2^{-20}$ | 0.49 | 0.68 | 0.69 | 0.62 | 0.62 | 0.64 |
| $p^N_{comp}$ | 0.61 | 0.69 | 0.69 | 0.62 | 0.62 | 0.64 |

Table 5: Computed orders of convergence $p^N_{\varepsilon,comp}$, $p^N_{comp}$ for $\frac{1}{V^*}(V_\varepsilon - V_B^{8192})$ where $V_\varepsilon$ is generated by $(A^{\mathbf{N}}_\varepsilon)$ for various values of $\varepsilon$, $N$ and $v_i$=0.3.

Table 6 indicate the order of convergence for $U_\varepsilon$ is at least 0.8 for $v_i = -0.3$ and all Reynolds.

| $\varepsilon \backslash N$ | 8 | 16 | 32 | 64 | 128 | 256 |
|---|---|---|---|---|---|---|
| $2^{-0}$ | -0.23 | 0.33 | 0.78 | 0.88 | 0.94 | 0.80 |
| $2^{-2}$ | 0.67 | 0.80 | 0.90 | 0.95 | 0.96 | 0.96 |
| $2^{-4}$ | 1.25 | 1.11 | 1.05 | 1.02 | 1.00 | 0.99 |
| $2^{-6}$ | 1.07 | 0.92 | 0.90 | 1.05 | 1.02 | 1.00 |
| $2^{-8}$ | 1.08 | 1.13 | 0.86 | 0.84 | 0.85 | 0.85 |
| . | . | . | . | . | . | . |
| $2^{-20}$ | 0.64 | 0.77 | 0.83 | 0.84 | 0.85 | 0.85 |
| $p^N_{comp}$ | 1.08 | 1.13 | 0.86 | 0.84 | 0.85 | 0.85 |

Table 6: Computed orders of convergence $p^N_{\varepsilon,comp}$, $p^N_{comp}$ for $U_\varepsilon - U_B^{8192}$ where $U_\varepsilon$ is generated by $(A^{\mathbf{N}}_\varepsilon)$ for various values of $\varepsilon$, $N$ and $v_i$=-0.3.

The results in tables 1 - 6 indicate that the direct numerical method is Reynolds uniform for the scaled velocity components with $v_i = -0.3$ and $v_i = 0.3$, thus we can guarantee accuracy for arbitrary Reynolds.

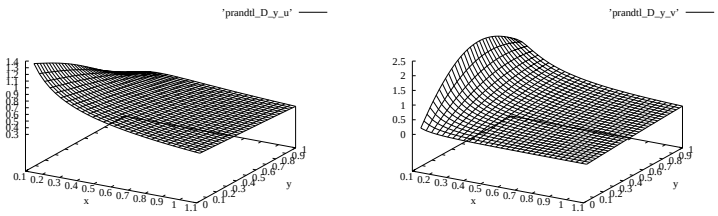


Figure 8: Graphs of $\sqrt{\varepsilon}(D_y^- U_\varepsilon)$ and $D_y^- V_\varepsilon$ for $\varepsilon = 1.0$, N=32 and $v_i = 0.3$.

Graphs of the computed scaled derivatives generated by $(A_\varepsilon^{\mathbf{N}})$ applied to $P_\varepsilon$ are given for N=32 and $\varepsilon = 1.0$ and $2^{-12}$ with $v_i = 0.3$ are given by figs 8 and 9. In figure 8 we see for small Reynolds the graphs for $\sqrt{\varepsilon}(D_y^- U_\varepsilon)$ and $D_y^- V_\varepsilon$ are smooth, with activity near $\Gamma_L$.

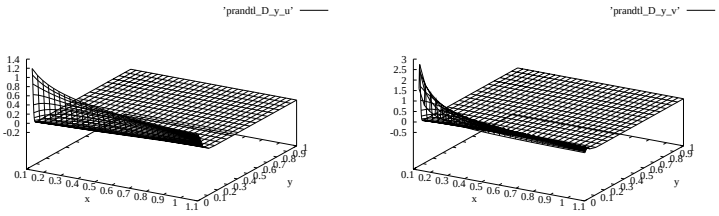


Figure 9: Graphs of $\sqrt{\varepsilon}(D_y^- U_\varepsilon)$ and $D_y^- V_\varepsilon$ for $\varepsilon = 2^{-12}$, N=32 and $v_i = 0.3$.

Figure 9 shows that the area of most activity is along the plate in the boundary layer and close to the leading edge for $\sqrt{\varepsilon} D_y^- U_\varepsilon$ and $D_y^- V_\varepsilon$ for $v_i = 0.3$. Tables 7 - 8 show the errors for the scaled derivatives $\sqrt{\varepsilon} D_y^- U_\varepsilon$ and $D_y^- V_\varepsilon$ for $v_i = 0.3$, as before the error stabilises as Reynolds increases.

| $\varepsilon \backslash N$ | 8 | 16 | 32 | 64 | 128 | 256 | 512 |
|---|---|---|---|---|---|---|---|
| $2^{-0}$ | 9.50e-02 | 4.78e-02 | 2.41e-02 | 1.23e-02 | 6.32e-03 | 3.35e-03 | 1.86e-03 |
| $2^{-2}$ | 1.87e-01 | 9.50e-02 | 4.78e-02 | 2.41e-02 | 1.23e-02 | 6.32e-03 | 3.35e-03 |
| $2^{-4}$ | 3.21e-01 | 1.87e-01 | 9.50e-02 | 4.78e-02 | 2.41e-02 | 1.23e-02 | 6.32e-03 |
| $2^{-6}$ | 3.37e-01 | 2.59e-01 | 1.63e-01 | 9.50e-02 | 4.78e-02 | 2.41e-02 | 1.23e-02 |
| $2^{-8}$ | 3.37e-01 | 2.59e-01 | 1.63e-01 | 9.89e-02 | 5.78e-02 | 3.33e-02 | 1.89e-02 |
| $2^{-10}$ | 3.37e-01 | 2.59e-01 | 1.63e-01 | 9.89e-02 | 5.78e-02 | 3.33e-02 | 1.89e-02 |
| . | . | . | . | . | . | . | . |
| $2^{-20}$ | 3.37e-01 | 2.59e-01 | 1.63e-01 | 9.89e-02 | 5.78e-02 | 3.33e-02 | 1.89e-02 |
| $E^N$ | 3.37e-01 | 2.59e-01 | 1.63e-01 | 9.89e-02 | 5.78e-02 | 3.33e-02 | 1.89e-02 |

Table 7: Computed maximum pointwise scaled error $\sqrt{\varepsilon}||D_y^- U_\varepsilon - D_y U_B^{8192}||_{\overline{\Omega_\varepsilon^N}/\Gamma_L}$ where $U_\varepsilon$ is generated by $(A_\varepsilon^{\mathbf{N}})$ for various values of $\varepsilon$, $N$ and $v_i$=0.3.

| $\varepsilon \backslash N$ | 8 | 16 | 32 | 64 | 128 | 256 | 512 |
|---|---|---|---|---|---|---|---|
| $2^{-0}$ | 5.29e-01 | 3.89e-01 | 2.32e-01 | 1.19e-01 | 6.02e-02 | 2.98e-02 | 1.57e-02 |
| $2^{-2}$ | 7.50e-01 | 5.44e-01 | 3.31e-01 | 1.87e-01 | 1.04e-01 | 5.91e-02 | 3.47e-02 |
| $2^{-4}$ | 1.30e+00 | 8.79e-01 | 5.35e-01 | 3.13e-01 | 1.84e-01 | 1.09e-01 | 6.52e-02 |
| $2^{-6}$ | 1.37e+00 | 1.25e+00 | 9.17e-01 | 6.14e-01 | 3.60e-01 | 2.15e-01 | 1.29e-01 |
| $2^{-8}$ | 1.37e+00 | 1.25e+00 | 9.17e-01 | 6.40e-01 | 4.41e-01 | 3.02e-01 | 2.04e-01 |
| . | . | . | . | . | . | . | . | . |
| $2^{-20}$ | 1.36e+00 | 1.25e+00 | 9.16e-01 | 6.40e-01 | 4.41e-01 | 3.03e-01 | 2.04e-01 |
| $E^N$ | 1.37e+00 | 1.25e+00 | 9.17e-01 | 6.40e-01 | 4.41e-01 | 3.03e-01 | 2.04e-01 |

Table 8: Computed maximum pointwise error $||D_y^- V_\varepsilon - D_y V_B^{8192}||_{\overline{\Omega_\varepsilon^N}}$ where $V_\varepsilon$ is generated by $(A_\varepsilon^{\mathbf{N}})$ for various values of $\varepsilon$, $N$ and $v_i$=0.3.

For small Reynolds the errors are evenly distributed thought out the domain with the largest occurring in the region of $\Gamma_L$ (fig 10).

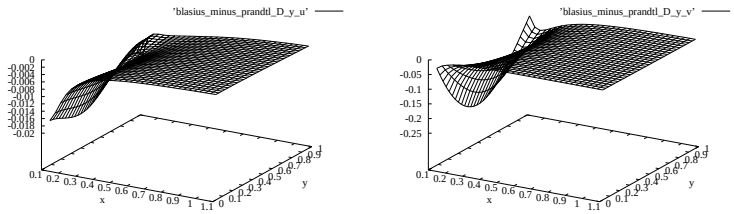


Figure 10: Graphs of $\sqrt{\varepsilon}(D_y^- U_\varepsilon - D_y U_B^{8192})$ and $D_y^- V_\varepsilon - D_y V_B^{8192}$ for $\varepsilon = 1.0$, N=32 and $v_i = 0.3$.

Figure 11 displays the errors of $\sqrt{\varepsilon} D_y^- U_\varepsilon$ and $D_y^- V_\varepsilon$ for N=32 and $\varepsilon = 2^{-12}$ with $v_i = 0.3$, the error is contained within the boundary layer with the largest error arising at the points closest to the leading edge.

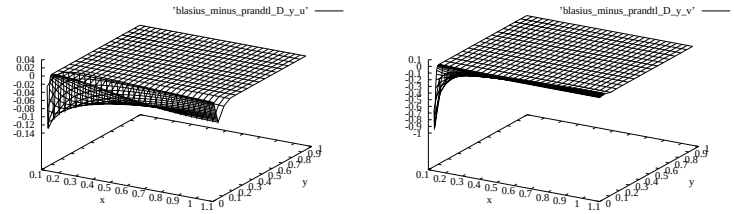


Figure 11: Graphs of $\sqrt{\varepsilon}(D_y^- U_\varepsilon - D_y U_B^{8192})$ and $D_y^- V_\varepsilon - D_y V_B^{8192}$ for $\varepsilon = 2^{-12}$, N=32 and $v_i = 0.3$.

Tables 9 - 10 show the order of convergences for $D_y^- V_\varepsilon$ and $\sqrt{\varepsilon} D_y^- U_\varepsilon$ for various N and Reynolds with $v_i = 0.3$.

| $\varepsilon \backslash N$ | 8 | 16 | 32 | 64 | 128 | 256 |
|---|---|---|---|---|---|---|
| $2^{-0}$ | 0.99 | 0.99 | 0.98 | 0.96 | 0.92 | 0.84 |
| $2^{-2}$ | 0.98 | 0.99 | 0.99 | 0.98 | 0.96 | 0.92 |
| $2^{-4}$ | 0.78 | 0.98 | 0.99 | 0.99 | 0.98 | 0.96 |
| $2^{-6}$ | 0.38 | 0.66 | 0.78 | 0.99 | 0.99 | 0.98 |
| $2^{-8}$ | 0.38 | 0.66 | 0.72 | 0.77 | 0.80 | 0.82 |
| . | . | . | . | . | . | . |
| $2^{-20}$ | 0.38 | 0.66 | 0.72 | 0.77 | 0.80 | 0.82 |
| $p^N_{comp}$ | 0.38 | 0.66 | 0.72 | 0.77 | 0.80 | 0.82 |

Table 9: Computed orders of convergence $p^N_{\varepsilon,comp}$, $p^N_{comp}$ for $\sqrt{\varepsilon}(D_y^- U_\varepsilon - D_y U_B^{8192})$ where $U_\varepsilon$ is generated by $(A_\varepsilon^{\mathbf{N}})$ for various values of $\varepsilon$, $N$ and $v_i$=0.3.

From table 9 it can be read that $\sqrt{\varepsilon} D_y^- U_\varepsilon$ for $v_i = 0.3$, has an order of convergence no less than 0.6 for $N \geq 16$.

| $\varepsilon \backslash N$ | 8 | 16 | 32 | 64 | 128 | 256 |
|---|---|---|---|---|---|---|
| $2^{-0}$ | 0.44 | 0.74 | 0.96 | 0.99 | 1.01 | 0.92 |
| $2^{-2}$ | 0.46 | 0.72 | 0.83 | 0.85 | 0.81 | 0.77 |
| $2^{-4}$ | 0.56 | 0.72 | 0.77 | 0.77 | 0.75 | 0.74 |
| $2^{-6}$ | 0.14 | 0.44 | 0.58 | 0.77 | 0.74 | 0.74 |
| $2^{-8}$ | 0.13 | 0.44 | 0.52 | 0.54 | 0.55 | 0.57 |
| . | . | . | . | . | . | . |
| $2^{-20}$ | 0.12 | 0.44 | 0.52 | 0.54 | 0.54 | 0.57 |
| $p^N_{comp}$ | 0.14 | 0.44 | 0.52 | 0.54 | 0.54 | 0.57 |

Table 10: Computed orders of convergence $p^N_{\varepsilon,comp}$, $p^N_{comp}$ for $D_y^- V_\varepsilon - D_y V_B^{8192}$ where $V_\varepsilon$ is generated by $(A_\varepsilon^{\mathbf{N}})$ for various values of $\varepsilon$, $N$ and $v_i$=0.3.

From table 10 it can be read that $D_y^- V_\varepsilon$ for $v_i = 0.3$, has an order of convergence no less than 0.5 for $N \geq 32$.
Tables 7 - 10 indicate that the direct numerical method is Reynolds uniform for $\sqrt{\varepsilon} D_y^- U_\varepsilon$ and $D_y^- V_\varepsilon$ for $v_i = 0.3$, this result also holds for the case when $v_i = -0.3$.

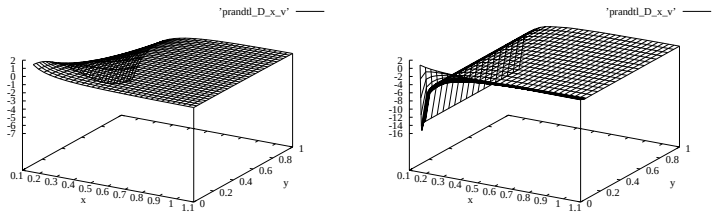


Figure 12: Graphs of $\frac{1}{V^*}(D_x^- V_\varepsilon)$ in the domain $\Omega_\varepsilon^N \backslash (X_1 \cup \Gamma_L)$ for $\varepsilon = 1.0$ and $\varepsilon = 2^{-12}$, N=32 and $v_i = 0.3$.

Figure 12 shows that the graphs for $\frac{1}{V^*} D_x^- V_\varepsilon$ for $N = 32$ and $\varepsilon = 1$ and $\varepsilon = 2^{-12}$ with $v_i = 0.3$, we can see that the leading edge has an obvious affect on

the region close to $\Gamma_L$ for both small and large Reynolds due to this singularity when dealing with the errors of $\frac{1}{V^*}D_x^- V_\varepsilon$ we only investigate the subdomain $(\overline{\Omega_\varepsilon^N} \cap [0.2, 1.1] \times [0, 1])$.

| $\varepsilon \backslash N$ | 8 | 16 | 32 | 64 | 128 | 256 | 512 |
|---|---|---|---|---|---|---|---|
| $2^{-0}$ | 2.49e+00 | 2.58e+00 | 1.17e+00 | 6.49e-01 | 3.43e-01 | 1.71e-01 | 8.76e-02 |
| $2^{-2}$ | 3.69e+00 | 3.10e+00 | 1.12e+00 | 5.89e-01 | 3.05e-01 | 1.49e-01 | 7.37e-02 |
| $2^{-4}$ | 1.07e+01 | 6.43e+00 | 1.52e+00 | 7.72e-01 | 3.89e-01 | 1.88e-01 | 9.23e-02 |
| $2^{-6}$ | 1.18e+01 | 1.14e+01 | 2.16e+00 | 1.16e+00 | 5.71e-01 | 2.68e-01 | 1.30e-01 |
| $2^{-8}$ | 1.22e+01 | 1.14e+01 | 2.16e+00 | 1.17e+00 | 6.33e-01 | 3.31e-01 | 1.74e-01 |
| . | . | . | . | . | . | . | . |
| $2^{-20}$ | 1.28e+01 | 1.15e+01 | 2.16e+00 | 1.17e+00 | 6.33e-01 | 3.31e-01 | 1.74e-01 |
| $E^N$ | 1.28e+01 | 1.15e+01 | 2.16e+00 | 1.17e+00 | 6.33e-01 | 3.31e-01 | 1.74e-01 |

Table 11: Computed maximum pointwise scaled error $V^{*-1}||D_x^- V_\varepsilon - D_x V_B^{8192}||$ in the subdomain $(\overline{\Omega_\varepsilon^N} \cap [0.2, 1.1] \times [0, 1])$ where $V_\varepsilon$ is generated by $(A_\varepsilon^{\mathbf{N}})$ for various values of $\varepsilon$, $N$ and $v_i$=0.3.

Table 11 gives the errors of the scaled derivative $\frac{1}{V^*}D_x^- V_\varepsilon$ for various values of N and Reynolds with $v_i = 0.3$ in the subdomain $(\overline{\Omega_\varepsilon^N} \cap [0.2, 1.1] \times [0, 1])$. The table show that the error stabilises as Reynolds increases.

| $\varepsilon \backslash N$ | 8 | 16 | 32 | 64 | 128 | 256 |
|---|---|---|---|---|---|---|
| $2^{-0}$ | -0.05 | 1.15 | 0.85 | 0.92 | 1.00 | 0.97 |
| $2^{-2}$ | 0.25 | 1.47 | 0.93 | 0.95 | 1.03 | 1.02 |
| $2^{-4}$ | 0.73 | 2.08 | 0.98 | 0.99 | 1.05 | 1.03 |
| $2^{-6}$ | 0.05 | 2.40 | 0.89 | 1.02 | 1.09 | 1.04 |
| $2^{-8}$ | 0.09 | 2.40 | 0.89 | 0.88 | 0.94 | 0.93 |
| . | . | . | . | . | . | . |
| $2^{-20}$ | 0.15 | 2.41 | 0.89 | 0.88 | 0.94 | 0.93 |
| $p_{comp}^N$ | 0.15 | 2.41 | 0.89 | 0.88 | 0.94 | 0.93 |

Table 12: Computed orders of convergence $p_{\varepsilon,comp}^N$, $p_{comp}^N$ for $\frac{1}{V^*}(D_x^- V_\varepsilon - D_x V_B^{8192})$ in the subdomain $(\overline{\Omega_\varepsilon^N} \cap [0.2, 1.1] \times [0, 1])$ where $V_\varepsilon$ is generated by $(A_\varepsilon^{\mathbf{N}})$ for various values of $\varepsilon$, $N$ and $v_i$=0.3.

From table 12 it can be read that $\frac{1}{V^*}D_x^- V_\varepsilon$ for $v_i = 0.3$ has an order of convergence no less than 0.85 for $N \geq 16$.

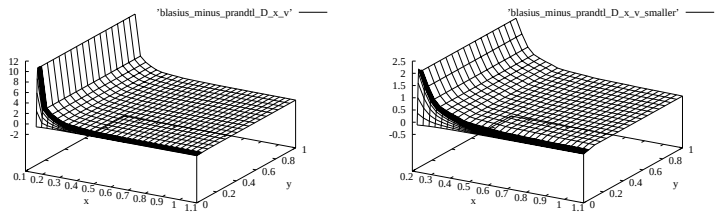


Figure 13: Graphs of $\frac{1}{V^*}(D_x^- V_\varepsilon - \delta_x V_B)$ in the domain $\Omega_\varepsilon^N \backslash (X_1 \cup \Gamma_L)$ and $\frac{1}{V^*}(D_x^- V_\varepsilon - \delta_x V_B)$ in the subdomain $(\overline{\Omega_\varepsilon^N} \cap [0.2, 1.1] \times [0, 1])$ for $\varepsilon = 2^{-12}$, N=32 and $v_i = 0.3$.

Figure 13 shows that on the domain $\Omega_\varepsilon^N \backslash (X_1 \cup \Gamma_L)$, the error for $D_x^- V_\varepsilon$ for $N = 32$ and $\varepsilon = 2^{-12}$ with $v_i = 0.3$ is large due to the leading edge singularity, by shifting down the x axis away from the singularity and looking at the subdomain $(\overline{\Omega_\varepsilon^N} \cap [0.2, 1.1] \times [0, 1])$ the error is significantly less.
Tables 11 - 12 indicate the within the subdomain the direct numerical method is Reynolds uniform for $\frac{1}{V^*} D_x^- V_\varepsilon$ for $v_i = -0.3$, this result also holds for $v_i = -0.3$.

# 6 Conclusion

We considered Prandtl's boundary layer equations for incompressible laminar flow past a plate with suction/blowing of the flow rate density $v_0(x) = -v_i 2^{-1/2} Re^{1/2} x^{-1/2}$, where the Reynolds number $Re$ can be arbitrarily large and $v_i$ is the intensity of the mass transfer with arbitrary values in the segment $[-.3, .3]$. When the Reynolds number is large the solution of this problem has a parabolic boundary layer at the surface of the plate excluding its leading edge. We constructed a direct numerical method for computing approximations to the solution of this problem using a piecewise uniform fitted mesh technique appropriate to the parabolic boundary layer. To validate this numerical method, the model Prandtl problem with self-similar solution was examined, for which a *reference* solution can be computed using the Blasius problem for a nonlinear ordinary differential equation. We considered the Prandtl problem in a finite rectangle excluding the leading edge of the plate for various values of $Re$ which can be arbitrary large and for some values of $v_i$, when meshes with different number of mesh points were used. To find reference solutions for the the velocity components and their derivatives with required accuracy, we solved the Blasius problem using a semi–analytical numerical method. By extensive numerical experiments we showed that the direct numerical method constructed in this paper allows us to approximate both the solution and its derivatives $Re$–uniformly for different values of $v_i$.

# Acknowledgements

This research was supported in part by the Enterprise Ireland grant SC-2000-070 and by the Russian Foundation for Basic Research under grant No. 01-01-01022.

# References


[1] P. Farrell, A Hegarty, J.J.H. Miller, E. O'Riordan, G.I. Shishkin, *Robust Computational Techniques for Boundary Layers*, CRC Press, (2000).

[2] H. Schlichting, *Boundary Layer Theory*, $7^{th}$ edition, McGraw Hill, (1951).

[3] D.J. Acheson, *Elementary Fluid Dynamics*, Oxford: Clarendon, (1990).

[4] D.F. Rogers, *Laminar Flow Analysis*, Cambridge University Press, (1992).

[5] B. Gahan, J.J.H. Miller, G.I. Shishkin, *Reynolds-uniform numerical method for Prandtl's problem with suction-blowing based on Blasius' approach*, Trinity College Dublin, Maths. Dept. Preprint TCDMATH 00-07 (2000).